

Experimental comparison of initiation of motion for submerged objects resting on fixed permeable and impermeable beds

Heng Wu,^{1,*} Carlo C. Zuniga Zamalloa,^{1,†} Blake J. Landry,^{2,‡} and Marcelo H. Garcia¹

¹*Ven Te Chow Hydrosystems Laboratory, Department of Civil and Environmental Engineering, University of Illinois at Urbana-Champaign, Urbana, Illinois 61801, USA*

²*Marine Geosciences Division, U.S. Naval Research Laboratory, Code 7434, Bldg. 1005, Stennis Space Center, Mississippi 39529, USA*



(Received 27 July 2018; published 22 January 2019)

Systematic experiments were conducted to study differences in the threshold flow conditions for initiation of motion of submerged objects (spheres and cylinders) resting on permeable and impermeable beds. The threshold flow conditions were characterized with the Shields parameter, which was estimated with upstream flow velocity measurements obtained with the particle image velocimetry (PIV) technique under conditions of unidirectional, open-channel flow in a laboratory flume. Flow-bed interface geometries were maintained across both permeable and impermeable bed experiments. Plotting the Shields parameter against the ratio of the particle size to bed roughness scale revealed clear differences between permeable and impermeable beds, including a larger Shields parameter value requirement to initiate motion on permeable beds than on impermeable ones, which is connected with the lower lift force on a permeable bed. Neglecting the presence of bed permeability can result in up to half an order of magnitude of variation in critical Shields parameter values. Experimental results also show that greater Shields parameter values are required to initiate the motion of a sphere than for a cylinder with identical diameter for large L/D ratio (L and D are the length and diameter of the cylinder). As the L/D ratio decreases, the cylinder approaches the sphere geometry, and the critical Shields parameter value is similar.

DOI: [10.1103/PhysRevFluids.4.013802](https://doi.org/10.1103/PhysRevFluids.4.013802)

I. INTRODUCTION

Sediment transport provides the critical connection between fluid dynamic processes and bed morphodynamics [1]. The importance of sediment transport ranges from small-scale sediment particle-to-particle interactions to macroscale bathymetric evolution, e.g., sand ripples and bars [2–5] and erosion or scour processes [6,7]. All mechanisms of sediment transport have incipient motion as their initial dynamic state, which is the instant at which a sediment particle resting on a bed begins moving due to the flow forces exerted on it.

The incipient motion of noncohesive sediment is particularly important since it defines the flow threshold for sediment mobility [8–12] and is crucial in understanding and engineering many natural processes. Such is the case for selecting armoring cobbles used for preventing scour

*hengwu2@illinois.edu

[†]Currently at National Research Council Research Associateship Program, Marine Geosciences Division, U.S. Naval Research Laboratory, Code 7434, Bldg. 1005, Stennis Space Center, Mississippi 39529, USA.

[‡]Formally at Ven Te Chow Hydrosystems Laboratory, Department of Civil and Environmental Engineering, University of Illinois at Urbana-Champaign, Urbana, Illinois 61801, USA.

around bridge footings [13], encouraging landscape evolution through bed load transport in rivers [14,15], determining the incipient motion and transport of underwater unexploded ordnance [16], or understanding nutrient delivery in ecological systems, as in the case of salmon eggs that have been laid in the hyporheic region of a river bed [17,18]. The importance of understanding these natural systems has driven extensive experimental study on incipient motion, culminating in the development of several theoretical models [19–30].

Many different approaches can be taken to assess the threshold of incipient motion of a single particle [19–30]. The analysis of the threshold for incipient motion in general involves force or moment balance of the fluid forces (drag and lift) exerted on the single particle and the submerged weight of the particle [31]. The approaches defining the threshold of incipient motion are roughly categorized as the deterministic and stochastic approaches [32]. The stochastic approach accounts for the significance of the fluctuations of the fluid forces arises from turbulence and argues that incipient motion could occur even when the mean flow is below the threshold to entrain particles [33]. The stochastic approach includes the force balance models and impulse models and treats the incipient motion as stochastic processes. The force balance models take the probability of particle entrainment as the probability of the fluid forces exceeding the submerged weight of the entrained particle [29,34–36]. Grass [30] considered the probability distribution of the flow shear stresses and the critical shear stress of single grain movement and proposed that the incipient motion occurs when the two probability distributions overlap. Lopez and Garcia [37] used a similar approach to assess risk of sediment erosion by a turbulent flow. The impulse approach argues that the magnitude of the instantaneous fluid forces exerted on the particle, combined with the duration of the fluids forces, dislodges the particle [25,26,38]. The stochastic approach emphasizes the role turbulence events play in particle entrainment [10,39–43].

The deterministic approach considers the fluid flow properties that are temporally (and spatially) averaged as the threshold for incipient motion. The models under deterministic approach are further categorized as the threshold flow velocity models and threshold bed shear stress models. Commonly, a force or moment balance of the forces acting on the object with respect to the contact point is performed to assess the threshold flow condition for incipient motion. The threshold velocity approach uses the time average of some type of flow velocity, such as at the particle level or depth averaged, as the threshold for incipient motion [28]. The threshold bed shear stress models were established by Shields [27] and use a dimensionless bed shear stress as the threshold for initiation of motion [19–23].

In the present work we adopted the threshold bed shear stress with moment balancing, which allows for critical shear stress to be related with measurable physical factors such as the local flow conditions or the relative particle size. The models implicitly assume impermeable beds and employ logarithmic velocity profiles although the presence of the logarithmic nature of the profiles remains in question [44]. Natural streams, however, often exhibit some degree of permeability, and there is no laboratory experimental evidence that shows the differences in initiation of motion that may arise due to the presence of bed permeability, which is the most common condition in nature.

This study experimentally explores the differences of initiation of motion requirements of spheres and cylinders when resting on a permeable versus an impermeable bed. In particular, focus is on the initiation of motion characterized by the Shields parameter versus particle to bed-particle size ratio. In the following section, a brief review of the current models for the initiation of motion of a single sphere is provided.

II. BACKGROUND

The mechanics of initiation of motion involve numerous of parameters, of which the most important ones are the fluid properties (density and viscosity), turbulent statistics of the flow (bed shear and turbulent stresses), particle characteristics such as density and shape, and particle size with respect to bed roughness [10,23]. The theoretical treatment of initiation of motion is widely based on single grain analysis, which describes the initiation of motion of a single sediment particle that

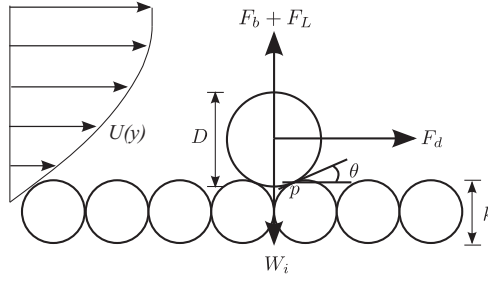


FIG. 1. The forces acting on a submerged object, where $U(y)$ is the streamwise flow velocity profile along the y direction, F_b is the Archimedean buoyant force, F_d is the fluid drag, W_i is the weight of the test object, D is the diameter of the object, ϕ is the contact angle between the object and the neighboring bed particles, and k is the length scale of the bed particles.

rests on a bed with the remaining bed particles potentially having different particle characteristics [19–22]. The mechanics of a precariously placed particle over a uniform bed involve an analysis of the forces acting on the particle. The forces result from the flow stresses, gravitational pull, and reactions due to the constraints posed by the bed topology [45,46]. Three forces acting on the grain are depicted in Fig. 1, where the initiation of motion occurs when the drag and lift force on the particle overcome the resistance effect of the immersed weight. A commonly used theoretical approach for the treatment of initiation of motion assumes that the mechanism of motion is driven by an imbalance of moments on a grain (e.g., a cylinder or sphere of diameter D) that pivots around a contact point P [45], as shown in Fig. 1.

For the scope of the present work, only one length scale for the bed particles, k , is considered (since the bed consists of spheres). The model formulation below is similar to that of Wiberg and Smith [21]. The drag force can be written as

$$F_D = \frac{1}{2} \rho c_D u_c^2 A_p, \quad (1)$$

where ρ is the density of the fluid, c_D is the drag coefficient of the particle, u_c is the flow velocity at the level of the centroid of the particle, and A_p is the projected area.

The lift force can be expressed as

$$F_L = \frac{1}{2} \rho c_L (u_T^2 - u_B^2) A_p, \quad (2)$$

where c_L is the lift coefficient of the particle, and u_T and u_B are the flow velocity at the level of the top and bottom of the particle, respectively.

The gravitational force, F_g , arising from the immersed weight, is given by

$$F_g = W_i - F_b = gV(\rho_s - \rho), \quad (3)$$

where W_i is the weight of the object, F_b is the buoyancy acting on the object, g is the acceleration of gravity, and V and ρ_s are the volume and density of the object, respectively.

Considering their respective moment arms for each force, the balance of moments is given by

$$F_D D \cos \phi = F_g D \sin \phi - F_L D \sin \phi, \quad (4)$$

where ϕ is the contact angle between the object and the neighboring bed particles. Rearrange the terms and we get

$$\frac{F_D}{F_g - F_L} = \tan \phi. \quad (5)$$

Scale the velocities at the level of the particle centroid, top, and bottom, with the shear velocity at the bed:

$$\hat{u}_c = \frac{u_c}{u_*}, \quad (6)$$

$$\hat{u}_T = \frac{u_T}{u_*}, \quad (7)$$

$$\hat{u}_B = \frac{u_B}{u_*}. \quad (8)$$

By substituting (1), (2), (3), and the scaled velocities into (5), the Shields parameter ψ can be determined as

$$\psi = \frac{\rho u_*^2}{(\rho_s - \rho)gD} = \frac{V}{A_p D} \frac{2}{c_D} \frac{1}{\hat{u}_c^2} \frac{\sin \phi}{\cos \phi + \frac{c_L}{c_D} \frac{u_T^2 - u_B^2}{u_c^2} \sin \phi}. \quad (9)$$

The ratio $\frac{V}{A_p D}$ is a factor based on the object shape and is $2/3$ for spheres and $\pi/4$ for cylinders. Assume small contact angle and simplify the above equation to get

$$\psi \sim \tan \phi = \frac{k/D}{\sqrt{1 + 2k/D}}. \quad (10)$$

For small k/D , the Shields parameter scales as $\psi \sim k/D$, which corresponds to the power law for an ideal system of spheres [23].

Previous pivoting models assumed logarithmic velocity profiles

$$\frac{U(y)}{u_*} = \frac{1}{\kappa} \ln \frac{y}{k}. \quad (11)$$

Evaluate the velocity at the particle level, $y = D/2$, and transform Eq. (9) to

$$\psi = \frac{\rho u_*^2}{(\rho_s - \rho)gD} = \frac{V}{A_p D} \frac{2}{c_D} \frac{\kappa^2}{[\ln(D/2k)]^2} \frac{\sin \phi}{\cos \phi + \frac{c_L}{c_D} \frac{u_T^2 - u_B^2}{u_c^2} \sin \phi}, \quad (12)$$

where κ is the von Kármán constant and equals 0.40. The equation matches the one presented by Wiberg and Smith [21] assuming negligible bed slope.

The analysis described above is the fundamental form of a precariously placed single particle exposed to the flow on a fixed uniform bed. Pivoting models focus on various aspects of pivoting. James [23] included more detail on the acting forces and extends the Shields parameter scaling (mentioned above) to an empirical equation with defined coefficients. Such detailed analysis is not restricted to spherical particles but also extends to particles of different shapes and angularity [20,23,45]. Most pivoting models account for the effect of pivoting behavior on a bed with nonuniform grain sizes. In addition, turbulence can be accounted for, albeit in a crude way, by introducing the Ω parameter defined as the ratio of the flow velocity at the particle level to the instantaneous velocity at the onset of initiation of motion [20]. The moment-balancing modeling approach of a single grain is known as a pivoting model. Alternatively, initiation of motion can be modeled as a sliding mechanism. For the sliding model, a force balance, rather than moments, is performed, and the reaction force opposing the initiation of motion is modeled as a frictional force with a friction angle. Both pivoting and sliding models are commonly used and offer good theoretical predictions [20–23]. However, the sliding model is preferred on a slope bed [47]. For the present study, the moment balance for a single grain on a uniform bed was employed.

Motivation

Regarding the aforementioned models and experiments, no systematic study has been conducted to explore the impact of the presence of bed permeability on initiation of motion. Turbulence statistics show that the presence of bed permeability plays a fundamental role [48]. Several studies

that show trends in frictional drag (a nondimensional form of the bed shear stress) at the flow-bed interface are clearly distinct for permeable and impermeable cases [49,50]. The well-established fully rough regime, where frictional drag is independent of Reynolds number [51], is expected to occur for large Reynolds number for impermeable rough walls. However, experimental work to date on permeable beds shows that for large Reynolds numbers, the frictional drag continues to increase with increasing Reynolds number, and therefore, no fully rough regime exists [49,50]. The differences in frictional drag and turbulence statistics between permeable and impermeable beds have been recently confirmed and further analyzed [48]. In addition to the drag and mean velocity profile differences, permeable beds yield lower lift force on objects close to them than impermeable beds due to the excess static pore pressure in the permeable bed [52]. Experiments for initiation of motion models have not systematically taken into consideration the differences in pivoting thresholds that may arise due to the presence of bed permeability [20–23]. Only one study, to the authors' knowledge, has involved modeling that considers how turbulent pressure fluctuations that originate in the permeable bed affect initiation of motion [24].

The turbulence model makes use of the fully rough, mean velocity profile equation, which contradicts the results that show no fully rough regime exists with a permeable bed [49,50]. Since frictional drag is a key term in the quantification of pivoting, the differences in the nondimensional turbulence statistics (e.g., mean velocity profile) and frictional drag between permeable and impermeable beds indicate there is a need to investigate the variations in initiation of motion thresholds between permeable and impermeable beds. The existing differences in the nondimensional mean velocity profile and frictional drag are keys to quantification of pivoting and warrant a closer examination.

The present study is a set of systematic experiments to address the effects of the presence of bed permeability on the initiation of motion of idealized submerged objects (i.e., cylinders and spheres). As a comparative experimental study to assess the effects of the presence of permeability on thresholds for initiation of motion, an ideal system was implemented, consisting of a fixed bed of uniform spheres on top of which free-moving particles (spheres and cylinders) were positioned. The experimental setup for this work is described in the following section.

III. EXPERIMENTAL SETUP AND PROCEDURE

Experiments were performed in a recirculating open channel with zero slope and a rectangular cross section of 0.35 m wide and 0.60 m high, known as the hyporheic flume [53,54]. The permeable bed comprised six cubically packed layers of uniform spheres (diameter $k = 3.8$ cm). The spheres were rigidly fixed on stainless steel rods to prevent motion of the bed during the experiments. The impermeable bed was created by placing a false PVC sheet on top of the permeable bed. Rows of hemispheres were glued to the false bottom to match the flow-bed interface geometry between permeable and impermeable conditions. The diameter of the hemisphere for the impermeable bed was equal to the diameter of the spheres in the permeable bed condition ($k = 3.8$ cm) [53,54]. The permeability of the bed was estimated with the Kozeny-Carman equation [44]

$$K = \frac{k^2(1 - \epsilon)^3}{180\epsilon^2}, \quad (13)$$

where ϵ is the solid volume fraction of the bed. The Kozeny-Carman equation estimates the permeability of the bed to be 3.28×10^{-6} m².

The tested idealized particles included 10 spheres and 20 cylinders of various sizes and densities. For the idealized spherical particles, two different materials were used, acrylic PMMA and acetal, with densities of 1.19 and 1.40 g/cm³, respectively. For each material, five different diameters of spherical particles were manufactured (1.9, 2.5, 3.8, 5.1, and 6.3 cm), resulting in a total of 10 spheres tested for initiation of motion. In addition to the spheres, 20 cylinders were also tested. Cylinders were fabricated using the same two materials and five diameters used for the spheres. The 20 cylinders can be grouped into two sets. The first set comprised 10 cylinders having constant length with five different diameters for each of the two materials. The second cylinder set comprised

TABLE I. The dimensions and densities of the test objects. D is the diameter, ρ_s is the density, k is the diameter of the bed sediment, and L is the length of the cylinders.

D (cm)	ρ_s (g/cm ³)	D/k	L (cm)	L/D
Cylinder set 1				
1.9	1.19	0.50	30.48	16.0
1.9	1.40	0.50	30.48	16.0
2.5	1.19	0.67	30.48	12.0
2.5	1.40	0.67	30.48	12.0
3.8	1.19	1.00	30.48	8.00
3.8	1.40	1.00	30.48	8.00
5.1	1.19	1.33	30.48	6.00
5.1	1.40	1.33	30.48	6.00
6.3	1.19	1.67	30.48	4.80
6.3	1.40	1.67	30.48	4.80
Cylinder set 2				
1.9	1.19	0.50	5.72	3.00
1.9	1.40	0.50	5.72	3.00
2.5	1.19	0.67	6.99	2.75
2.5	1.40	0.67	6.99	2.75
3.8	1.19	1.00	10.16	2.67
3.8	1.40	1.00	10.16	2.67
5.1	1.19	1.33	13.97	2.75
5.1	1.40	1.33	13.97	2.75
6.3	1.19	1.67	17.15	2.70
6.3	1.40	1.67	17.15	2.70
Sphere				
1.9	1.19	0.50	-	-
1.9	1.40	0.50	-	-
2.5	1.19	0.67	-	-
2.5	1.40	0.67	-	-
3.8	1.19	1.00	-	-
3.8	1.40	1.00	-	-
5.1	1.19	1.33	-	-
5.1	1.40	1.33	-	-
6.3	1.19	1.67	-	-
6.3	1.40	1.67	-	-

10 cylinders having five different lengths for each of the five different diameters to maintain a constant L/D ratio (2.7). For each size, cylinders of two different materials (acrylic PMMA and acetal) were tested. Refer to Table I for detailed test particle characteristics.

A two-dimensional particle image velocimetry (PIV) system was implemented to measure the upstream streamwise and wall-normal flow velocities [55]. The PIV system comprised a New Wave Gemini Nd:YAG laser and a TSI 610035 synchronizer. The image pairs were acquired by a Power View 4MP Plus CCD camera with a resolution of 2048×2048 pixels and a field of view of approximately $20 \text{ cm} \times 20 \text{ cm}$. The time lapse between straddling frames ranged between 1000 and 3000 ms (depending on the experimental flow conditions) but was fixed for each trial. The laser sheet was oriented into the test section through a transparent visor on the top of the open channel (see Fig. 2). The visor prevented free surface waves from interfering with the laser sheet, and the flow disturbances were minimized due to the hydrodynamic edge on both upstream and downstream sides. Silver-coated hollow glass spheres with a mean diameter of $10 \mu\text{m}$ and an average specific gravity of 1.70 were used as seeding.

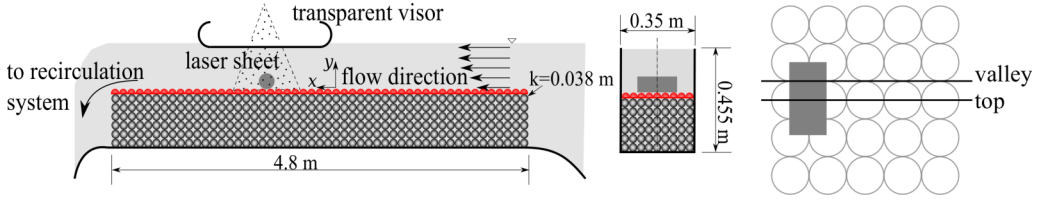


FIG. 2. Illustration of experimental setup for the impermeable bed condition. (Left image) Profile view of the facility. The PIV measurement window is denoted as the shaded box. (Middle image) Cross section view of the flume. The test object on the bed is a cylinder in the illustration. (Right image) A close top view of the test section, showing the positioning of the laser sheet.

The following experimental procedure was used for each trial:

- (1) The idealized particle was placed in the test section without constraint on its motion.
- (2) Starting from a quiescent flow, the flow rate was gradually increased. At each flow rate, the reaction of the test object was observed for a few minutes.
- (3) Depending on the reaction of the object to the flow:

Case a: if the object did not move (even when it wobbled), the flow rate was further increased by a small increment.

Case b: provided the object wobbled and then displaced by the flow, the flow rate was reduced, the object was repositioned to the initial position, and the flow rate was iterated to refine the threshold flow rate.

- (4) After determining the threshold flow rate, the object was fixed in place, and PIV measurements of the flow field were acquired.

The velocity fields contained the streamwise (u) and wall-normal (v) components on a vertical plane perpendicular to the lateral direction, as shown in Fig. 2. The velocity fields were measured at two lateral positions. One passed through the top of the bed particles and the centerline of the flume. The other slice at the valley of the bed particles with an offset to the centerline of the flume of one radius of the bed particle.

For each experimental trial, 2500 image pairs were acquired at 7.25 Hz. Image processing to obtain the instantaneous velocity fields was accomplished using the TSI software Insight 4G. Within Insight 4G, a square grid was applied to the images to divide the images into interrogation windows. In the interrogation windows, the particles between the image pairs were correlated, and the average displacement of the particles in each window was determined in pixel units. Immediately after acquiring the images in one trial, the image units were converted to physical displacements (meters) by using the standard TSI PIV calibration target. Last, knowing the time separation of the instantaneous velocity fields of each image pair, the flow velocities were obtained (m/s). A sample of the mean streamwise velocity field is shown in Fig. 3(a).

To calculate the Shields parameter, the bed shear stress was approximated by the sum of Reynolds stress τ_R , form-induced shear τ_f , and viscous stress τ_v at the tangent surface of the bed with the double-averaging method [56]:

$$\tau_b = \tau_R + \tau_f + \tau_v. \quad (14)$$

The Reynolds stress τ_R , form-induced shear τ_f , and viscous stress τ_v are defined as

$$\tau_R = -\rho \langle \overline{u'v'} \rangle, \quad (15)$$

$$\tau_f = -\rho \langle \tilde{u}\tilde{v} \rangle, \quad (16)$$

$$\tau_v = \rho \nu \left\langle \frac{\partial \bar{u}}{\partial z} \right\rangle, \quad (17)$$

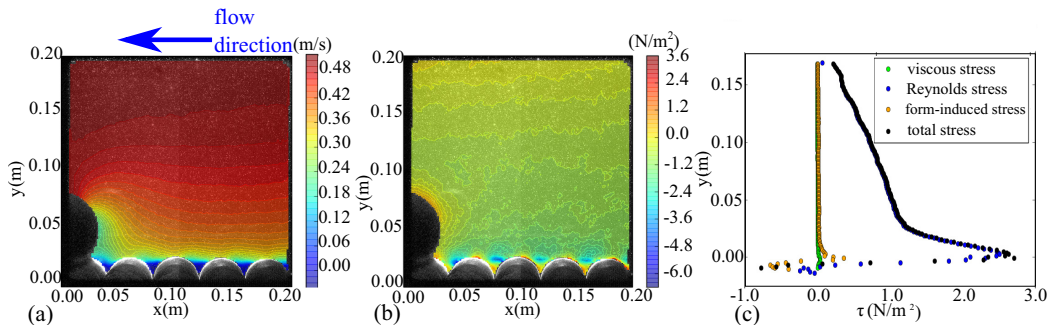


FIG. 3. (a) The mean velocity field measured at the top of the bed particles, (b) the Reynolds stress field measured at the top of the bed particles, and (c) viscous stress, τ_v , Reynolds stress τ_R , form-induced shear τ_f , and total stress τ_t profiles (defined as the origin of y axis at the tangent surface of the bed) for the case of the sphere with a diameter of 6.3 cm and specific density of 1.40 on a permeable bed.

where u' and v' are the velocity fluctuations

$$u' = u - \bar{u}; \quad v' = v - \bar{v}, \quad (18)$$

the angle brackets denote the spatial average in the x - z plane, and the overbar denotes the temporal average. The tilde denotes the spatial velocity fluctuation

$$\tilde{u} = \bar{u} - \langle \bar{u} \rangle; \quad \tilde{v} = \bar{v} - \langle \bar{v} \rangle. \quad (19)$$

To obtain the shear stress profile, the spatial average in the streamwise direction was over a width of one bed particle diameter which is located three bed particle diameters (11.4 cm) upstream of the test object. The spatial average in the lateral direction is a direct average of the top and valley slice. The bed shear stress was approximated as the total shear stress at the tangent surface of the bed. A sample of the Reynolds stress field from the slice passing through the top of the bed particle and profiles of the three components of the shear stress is shown in Figs. 3(b) and 3(c).

IV. RESULTS AND DISCUSSION

The Shields parameter, ψ , was plotted as a function of the particle-size ratio, D/k , for the cases of permeable and impermeable bed with spheres and cylinders. Figure 4(a) illustrates the relationship between the Shields parameter and the ratio of the particle size to bed roughness scale, D/k , for spherical particles. The relationship is an inverse power law, which follows the trend of previous observations [23]. Although the present arrangement of the idealized bed particles was different herein (i.e., cubic packing) from prior random packing experiments [23], there is no significant differences in the trend between the results. In addition, Fig. 4(a) shows the Shields parameter for the spherical particles on a permeable bed was higher compared to the impermeable bed.

Similarly, in Figs. 4(b) and 4(c), the Shields parameter for cylindrical objects is plotted against the ratio of the particle size to bed roughness scale, D/k . The inverse power law relationship between the Shields parameter and D/k still persists. As observed with the spherical test particles, the Shields parameter was lower under the condition of an impermeable bed than that of a permeable bed.

The effect that particle shape (spheres and cylinders) and bed permeability have on the thresholds for initiation of motion can be experimentally obtained by examining the relationship between the Shields parameter, ψ , as a function of D/k . For fixed interface topology, Fig. 4 illustrates that greater values of Shields parameter are required to initiate the motion of an idealized particle when it is resting on a permeable bed versus an impermeable bed. Initially, the result seems counterintuitive

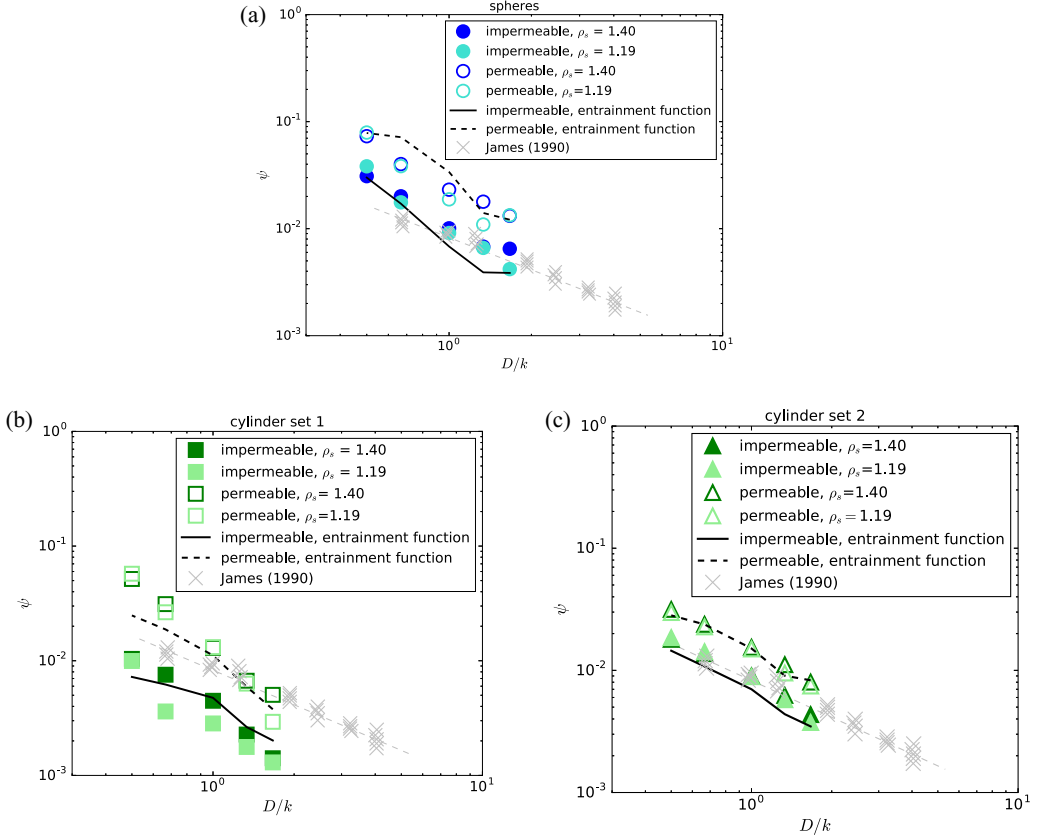


FIG. 4. For (a) spheres, (b) cylinder set 1 (constant length), and (c) cylinder set 2 (constant L/D ratio), the threshold Shields parameter was plotted against the particle-size ratio, D/k , value, compared with James [23]. Open and filled symbols stand for permeable and impermeable condition, respectively. The solid and dashed line are the entrainment equation [Eq. (9)] corresponds to impermeable and permeable condition, respectively. The dashed light gray line with a minus one slope is superimposed for comparison. Refer to Table I for the specifics of the objects.

since a permeable bed tends to have higher wall shear stress for a fixed interface roughness [49]. Under the aforementioned consideration, the increase in bed shear can result in the particle initiating motion earlier on a permeable bed than an impermeable bed. However, results show that permeable beds present a higher Shields parameter than impermeable ones. We suspect the trend is due to the lift force created by the flow around the idealized particle. Prior literature has shown that permeable beds yield a lower lift force on objects close to them than impermeable beds due to the excess static pore pressure in the permeable bed [52]. The lift force originates from the flow velocity difference across the particle and scales as $(u_T^2 - u_B^2)$ [Eq. (2)] where u_T is the double-averaged upstream flow velocity at the level of the top of the object and u_B was approximated by the double-averaged upstream flow velocity at the tangent surface of the bed. To compare the lift exerted on an object at incipient motion on permeable and impermeable beds, the ratio $\frac{u_T^2 - u_B^2}{u_*^2}$ was plotted against the bulk Reynolds number, $Re = \frac{DU_\infty}{\nu}$, where U_∞ denotes the free stream flow velocity, in Fig. 5. The plot shows that the $\frac{u_T^2 - u_B^2}{u_*^2}$ ratio is higher for objects resting on an impermeable bed under the same bulk Reynolds number. The lower $\frac{u_T^2 - u_B^2}{u_*^2}$ ratio across an object on a permeable bed can be attributed to the nonzero flow velocity inside the permeable bed underneath the object, while the

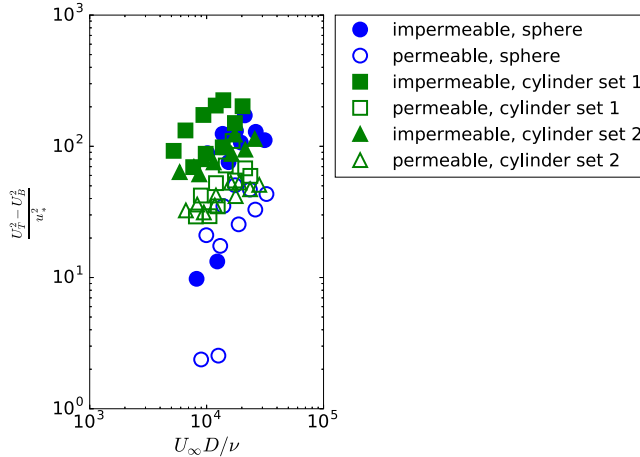


FIG. 5. The $\frac{U_f^2 - U_b^2}{u_*^2}$ ratio was plotted against the bulk Reynolds number, $Re = \frac{DU_\infty}{\nu}$ to show that the lift is smaller for objects resting on a permeable bed than on an impermeable one. Filled and open symbols stand for the impermeable and permeable conditions, respectively.

impermeable bed imposes a no-slip boundary condition at the bed. Thus, an object experiences larger lift force when resting on an impermeable bed than on a permeable one. This results in a lower shear stress required to initiate motion of an object on an impermeable bed and, therefore, yields a lower threshold Shields parameter.

The model from (9) was plotted in Fig. 4 for comparison. In (9), the value of \hat{u}_c^2 and $\frac{u_f^2 - u_b^2}{u_c^2}$ was from direct measurement in the experiments. The drag coefficient for the spheres was considered to be a constant of 0.47 because the flow was fully turbulent and the range of the Reynolds number was narrow. For the cylinders, the drag coefficient depends strongly on the length to diameter ratio, L/D , where L is the length of the cylinder. For the L/D ratio of the tested cylinders, the drag coefficient ranged from 0.70 to 0.89 [57,58]. The c_L/c_D ratio bears a wide range of values from 0.17 to 2.39 due to the difficulties in measuring the lift force [59–63]. In this study, the c_L/c_D values was estimated to be between 1.22 and 2.39 depending on the protrusion of the object out of the bed for the permeable bed condition [63]. Experiments showed that the lift force is higher on an impermeable bed than on a permeable one due to the absence of the excess pore pressure in a permeable bed. The increase in lift force on an impermeable bed causes the c_L/c_D ratio to be 1.24 to 1.42 times higher than that on a permeable one [52]. Here we approximated the c_L/c_D on an impermeable bed to be 1.24 times that of a permeable one. In Fig. 4 differences in the $\frac{u_f^2 - u_b^2}{u_c^2}$ ratio and the magnification of the c_L/c_D ratio on an impermeable bed separated the curves for the Shields parameter on permeable and impermeable beds. The prediction from (9) agreed with the Shields parameter from the experiments. Including the lift force in the form of Eq. (2) into the model and combining the lower lift coefficients on permeable beds gave a good estimation of the discrepancy of the Shields parameter of the Shields parameter on a permeable bed from an impermeable one.

Another significant feature was found in the relationships between ψ and D/k . For the same D/k ratio, the Shields parameter value is greater for spheres than it is for cylinder set 1, which have larger L/D values; see Fig. 6. This is persistent across the two particle densities (acrylic PMMA and acetal) and the permeable and impermeable beds. The increase in Shields parameter values for spheres when compared to constant length cylinders is attributed to differences in the surface shape of the objects. The flat sides of the cylinders induce flow separation earlier than for the case of spheres. Also, the drag coefficient for a cylinder is larger than that of a sphere, e.g., 0.47 for a sphere and 0.70 to 0.89 for a cylinder when away from a solid boundary. Consequently, a sphere requires

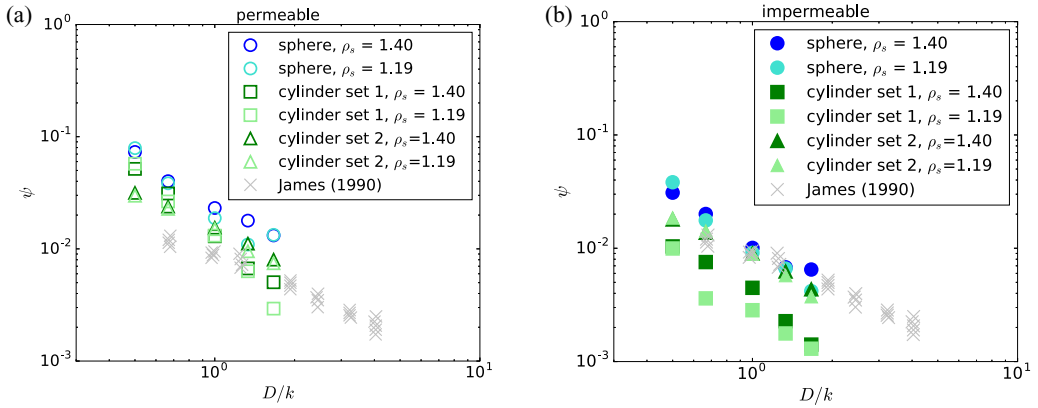


FIG. 6. For (a) permeable and (b) impermeable cases, the threshold Shields parameter for cylinders and spheres were plotted for different values of the ratio of the particle size to bed roughness scale, D/k . See Table I for the specifics of cylinder sets 1 and 2.

larger stresses to initiate motion than a cylinder, resulting in a cylinder perceiving more drag than a sphere for a given flow rate. Figure 6 depicts that the Shields parameter of cylinder set 2 (L/D fixed at 2.7) is comparable to the spheres, suggesting that the L/D ratio influences the threshold for initiation of motion. The effect of the L/D ratio is illustrated in Fig. 7 as the Shields parameter is plotted with respect to L/D .

In Fig. 7 the Shields parameter increases as the L/D ratio decreases. The trend should be attributed to that for smaller L/D ratios the shape of a cylinder is closer to a sphere in terms of the projected area. The inverse relationship between the Shields parameter and the L/D ratio is especially apparent for the impermeable bed case. This should be associated with the higher lift of the object on impermeable beds. The drag and lift coefficients depend strongly on the L/D ratio [57,58]. With higher lift imposed on an object resting on an impermeable bed, the L/D ratio will be more influential than on permeable beds. In addition to the effect of L/D ratios, Fig. 7 shows

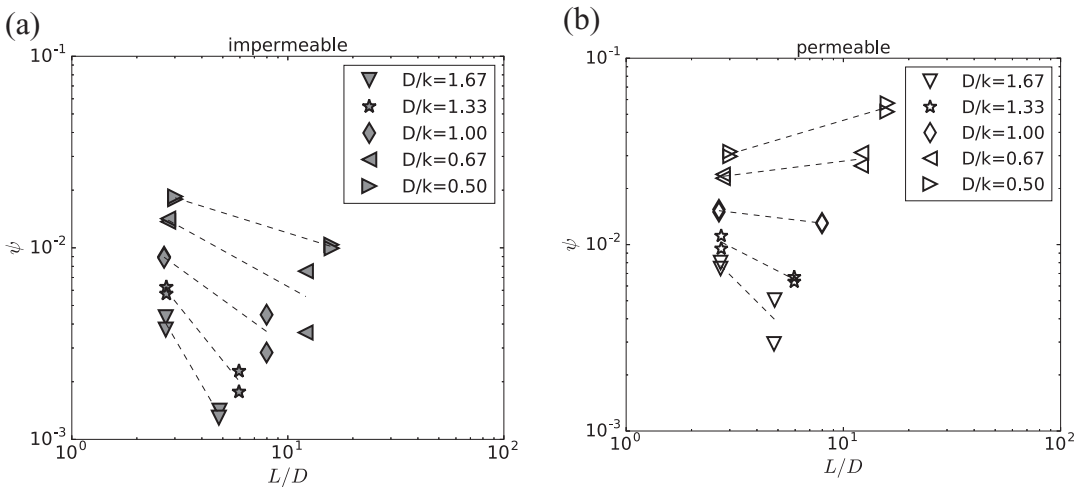


FIG. 7. For (a) impermeable and (b) permeable cases, the Shields parameter for cylinder are plotted against the length over diameter ratio, L/D , for different ratio of the particle size to bed roughness scale, D/k . See Table I for the specifics of cylinder sets 1 and 2.

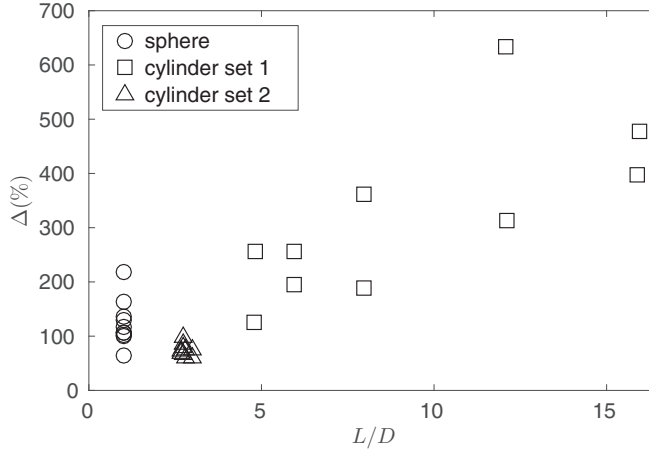


FIG. 8. The relative variation, Δ , was plotted against the L/D ratio. The square and triangle symbol denote cylinder set 1 and 2, respectively. The relative variation for spheres is denoted with circle symbols. Although the L/D ratio of spheres is not defined in Table I, a value of $L/D \sim 1$ is assigned to the spheres to illustrate the trend despite of the shape effect. The open symbol does not denote the permeable condition in this plot. See Table I for the specifics of the test objects.

that the Shields parameter, ψ , increases with D/k , indicating that initiation of motion of cylinders with smaller diameters requires higher flow rates for similar L/D ratios due to the hiding effect of smaller particles. Furthermore, the L/D ratio also affects the variation in the Shields parameter due to the presence of bed permeability.

To quantify the effect of the presence of a permeable bed on initiation of motion thresholds of the test objects, the permeability variation for each object was computed as

$$\Delta = (\psi_{\text{permeable}} - \psi_{\text{impermeable}}) / \psi_{\text{permeable}}, \quad (20)$$

where Δ is the variation in Shields parameter due to the permeability, and $\psi_{\text{permeable}}$ and $\psi_{\text{impermeable}}$ are the Shields parameter of an object resting on a permeable and impermeable bed, respectively. The variation, Δ , is plotted against L/D in Fig. 8, which illustrates a clear trend of increasing Δ with increasing L/D ratio. The results suggest that the L/D ratio is a crucial factor in the drag and lift coefficients of a cylinder since the variation in Shields parameter can reach as high as half an order of magnitude if the presence of bed permeability is not accounted for. Although the L/D ratio is typically not defined for spheres, a value of $L/D \sim 1$ was assigned to sphere experiments to better illustrate the increasing variation, Δ , with the L/D ratio.

For comparison, the Shields diagram (Fig. 9) was also plotted with the theoretical predictions using Ref. [23] and other experimental data [64,65] for incipient motion on beds comprised of uniform size spheres. The two semiempirical model prediction curves correspond to the model for incipient motion of a single bed particle resting on beds composed of uniform sized spheres and natural mixed size sediments [23]. In Fig. 9 only the data corresponding to D/k equals one were plotted since the Shields diagram is for initiation of motion of a well-sorted sediment bed. The model prediction of the Shields curve associated with mixed size natural sediment is higher than that of a uniform sized sphere bed, which is connected with the sediment grain being less exposed [23]. The data points associated with an impermeable bed for spheres and cylinder set 2 match well the theoretical curve as it assumed a logarithmic velocity profile that is valid only for an impermeable rough bed. The Shields parameter for cylinder set 1 (larger L/D) on an impermeable bed is much lower than the theoretical value because the shape of the object deviates from a sediment grain due to its large L/D value. From the plot, for comparable shear Reynolds number, the Shields parameter corresponding to the case of a permeable bed is clearly greater than that for the impermeable case.

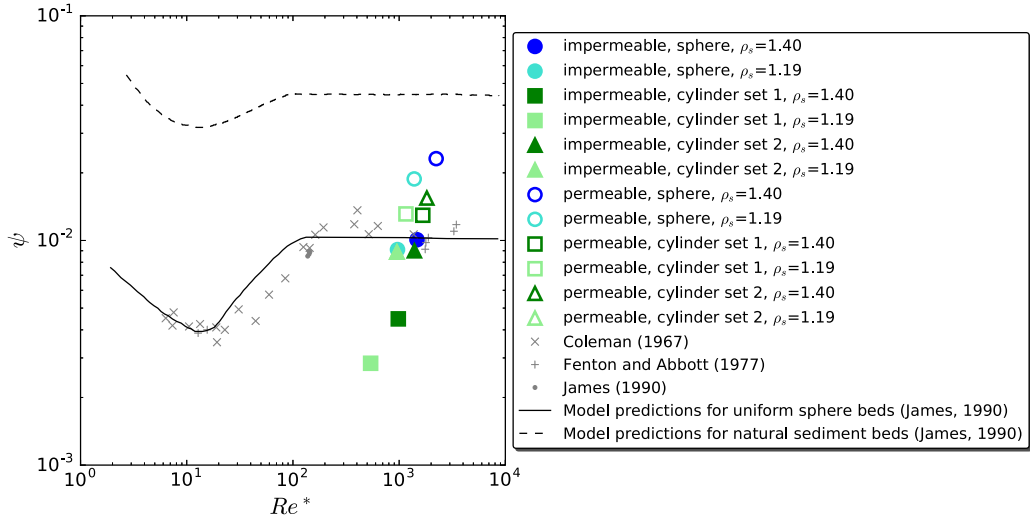


FIG. 9. Comparison of experimental results and the theoretical Shields curve for a single sphere on a bed of uniform spheres [23]. The square and triangular symbols denote cylinder sets 1 and 2, respectively. The spheres are denoted with circle symbols. Open and filled symbols stand for permeable and impermeable conditions, respectively.

V. SUMMARY

Prior experimental work has been conducted to explore differences between flows over permeable and impermeable beds [48]. However, there is a knowledge gap when assessing how the presence of bed permeability impacts initiation of motion of a single particle. Detailed laboratory experiments were conducted which comprised two-dimensional PIV measurements to resolve the flow field upstream of the submerged spheres and cylinders for the threshold flow condition at the initiation of motion. The Shields parameters for the idealized submerged objects were estimated from bed shear stresses and compared between different shapes on permeable and impermeable beds. The bed shear stresses were approximated by the sum of the Reynolds stress, form-induced stress, and viscous stress at the tangent surface of the bed with the double averaging method [56]. Experimental results show that larger Shields parameters are required to initiate motion of an object placed on a permeable bed compared to an impermeable bed. The increased Shields parameter can be connected with differences in the lift coefficient exerted on the particle. In addition to the effect of the presence of bed permeability, results illustrate that a greater Shields parameter is required to initiate the motion of a sphere than for a cylinder with identical diameter for large L/D ratios. As the L/D ratio decreases, the cylinder approaches the sphere geometry, and the Shields parameter value is similar. Finally, experiments show that neglecting bed permeability can result in up to half an order of magnitude of variation in Shields parameter values for threshold of motion.

ACKNOWLEDGMENTS

The authors are grateful for the support from the Strategic Environmental Research and Development Program (SERDP), Projects No. MR-2410 and No. MR-2320; and National Science Foundation, Grant No. EAR-1215879. Special thanks to Jorge E. San Juan Blanco for experimental assistance, Andrew Waratuke for helping with the experimental setup, and Stephen J. Gates, Sarah P. Wenzel, Dimitrios K. Fytanidis, Matthew J. Czapiga, and the reviewers for providing comments to improve the manuscript. The financial support of the junior author H.W. by the M. T. Geoffrey Yeh Endowed Chair of Civil Engineering is gratefully appreciated.

- [1] P. D. Komar, Entrainment of sediments from deposits of mixed grain sizes and densities, in *Advances in Fluvial Dynamics and Stratigraphy* (Wiley, Chichester, New York, 1996), pp. 127–181.
- [2] B. J. Landry, M. J. Hancock, and C.-C. Mei, Note on sediment sorting in a sandy bed under standing water waves, *Coastal Eng.* **54**, 694 (2007).
- [3] F. Pedocchi and M. H. Garcia, Ripple morphology under oscillatory flow: 1. Prediction, *J. Geophys. Res.: Oceans* **114**, C12014 (2009).
- [4] A. M. Penko, D. N. Slinn, and J. Calantoni, Model for mixture theory simulation of vortex sand ripple dynamics, *J. Waterway Port Coastal Ocean Eng.* **137**, 225 (2010).
- [5] F. Charru, B. Andreotti, and P. Claudin, Sand ripples and dunes, *Annu. Rev. Fluid Mech.* **45**, 469 (2013).
- [6] M. G. Kleinmans, J. R. F. W. Leuven, L. Braat, and A. Baar, Scour holes and ripples occur below the hydraulic smooth to rough transition of movable beds, *Sedimentology* **64**, 1381 (2017).
- [7] Y. A. Cataño-Lopera, B. J. Landy, and M. H. Garcia, Unstable flow structure around partially buried objects on a simulated river bed, *J. Hydroinf.* **19**, 31 (2017).
- [8] J. M. Buffington and D. R. Montgomery, A systematic analysis of eight decades of incipient motion studies, with special reference to gravel-bedded rivers, *Water Resour. Res.* **33**, 1993 (1997).
- [9] M. H. Garcia, E. M. Laursen, C. Michel, and J. M. Buffington, The legend of A. F. Shields, *J. Hydraul. Eng.* **126**, 718 (2000).
- [10] Y. Niño and M. H. Garcia, Experiments on particle-turbulence interactions in the near-wall region of an open channel flow: Implications for sediment transport, *J. Fluid Mech.* **326**, 285 (1996).
- [11] Y. Niño, F. Lopez, and M. H. Garcia, Threshold for particle entrainment into suspension, *Sedimentology* **50**, 247 (2003).
- [12] M. P. Lamb and J. G. Venditti, The grain size gap and abrupt gravel-sand transitions in rivers due to suspension fallout, *Geophys. Res. Lett.* **43**, 3777 (2016).
- [13] B. W. Melville and A. J. Sutherland, Design method for local scour at bridge piers, *J. Hydraul. Eng.* **114**, 1210 (1988).
- [14] M. P. Lamb, W. E. Dietrich, and L. S. Sklar, A model for fluvial bedrock incision by impacting suspended and bed load sediment, *J. Geophys. Res.: Earth Surf.* **113**, F03025 (2008).
- [15] A. R. Beer and J. M. Turowski, Bedload transport controls bedrock erosion under sediment-starved conditions, *Earth Surf. Dyn.* **3**, 291 (2015).
- [16] S. E. Rennie, A. Brandt, and C. T. Friedrichs, Initiation of motion and scour burial of objects underwater, *Ocean Eng.* **131**, 282 (2017).
- [17] M. D. Alexander and D. Caissie, Variability and comparison of hyporheic water temperatures and seepage fluxes in a small Atlantic salmon stream, *Ground Water* **41**, 72 (2003).
- [18] I. A. Malcolm, A. F. Youngson, and C. Soulsby, Survival of salmonid eggs in a degraded gravel-bed stream: Effects of groundwater-surface water interactions, *River Res. Appl.* **19**, 303 (2003).
- [19] S. Ikeda, Incipient motion of sand particles on side slopes, *J. Hydraul. Div.* **108**, 95 (1982).
- [20] P. D. Komar and Z. Li, Applications of grain-pivoting and sliding analyses to selective entrapment of gravel and to flow-competence evaluations, *Sedimentology* **35**, 681 (1988).
- [21] P. L. Wiberg and J. D. Smith, Calculations of the critical shear stress for motion of uniform and heterogeneous sediments, *Water Resour. Res.* **23**, 1471 (1987).
- [22] J. W. Kirchner, W. E. Dietrich, F. Iseya, and H. Ikeda, The variability of critical shear stress, friction angle, and grain protrusion in water-worked sediments, *Sedimentology* **37**, 647 (1990).
- [23] C. S. James, Prediction of entrainment conditions for nonuniform, noncohesive sediments, *J. Hydraul. Res.* **28**, 25 (1990).
- [24] S. Vollmer and M. G. Kleinmans, Predicting incipient motion, including the effect of turbulent pressure fluctuations in the bed, *Water Resour. Res.* **43**, W05410 (2007).
- [25] P. Diplas, C. L. Dancy, A. O. Celik, M. Valyrakis, K. Greer, and T. Akar, The role of impulse on the initiation of particle movement under turbulent flow conditions, *Science* **322**, 717 (2008).
- [26] M. Valyrakis, P. Diplas, C. L. Dancy, K. Greer, and A. O. Celik, Role of instantaneous force magnitude and duration on particle entrainment, *J. Geophys. Res.: Earth Surf.* **115**, F02006 (2010).
- [27] A. Shields, Application of similarity principles and turbulence research to bed-load movement, in W. P. Ott and I. C. Uchelen (translators), Mitt. Preuss. Versuchsanst., Berlin. Wasserbau Schiffbau. W. M. Kech

- Laboratory of Hydraulics and Water Resources, California Institute of Technology, Pasadena, CA, Report No. 167 (1936).
- [28] C. T. Yang, Incipient motion and sediment transport, *J. Hydraul. Div.* **99**, 1679 (1973).
- [29] H. A. Einstein, *The Bed-Load Function for Sediment Transportation in Open Channel Flows*, Technical Bulletin (US Department of Agriculture, Washington DC, USA, 1950), Vol. 1026.
- [30] A. J. Grass, Initial instability of fine bed sand, *J. Hydraul. Div.* **96**, 619 (1970).
- [31] V. A. Vanoni, *Sedimentation Engineering* (American Society of Civil Engineers, Reston, Virginia, USA, 2006).
- [32] S. Dey and S. Z. Ali, Advances in modeling of bed particle entrainment sheared by turbulent flow, *Phys. Fluids* **30**, 061301 (2018).
- [33] A. S. Paintal, Concept of critical shear stress in loose boundary open channels, *J. Hydraul. Res.* **9**, 91 (1971).
- [34] N.-S. Cheng and Y.-M. Chiew, Pickup probability for sediment entrainment, *J. Hydraul. Eng.* **124**, 232 (1998).
- [35] F.-C. Wu and Y.-C. Lin, Pickup probability of sediment under log-normal velocity distribution, *J. Hydraul. Eng.* **128**, 438 (2002).
- [36] F.-C. Wu and Y.-J. Chou, Rolling and lifting probabilities for sediment entrainment, *J. Hydraul. Eng.* **129**, 110 (2003).
- [37] F. Lopez and M. H. Garcia, Risk of sediment erosion and suspension in turbulent flows, *J. Hydraul. Eng.* **127**, 231 (2001).
- [38] A. O. Celik, P. Diplas, C. L. Dancey, and M. Valyrakis, Impulse and particle dislodgement under turbulent flow conditions, *Phys. Fluids* **22**, 046601 (2010).
- [39] A. Dwivedi, B. Melville, and A. Y. Shamseldin, Hydrodynamic forces generated on a spherical sediment particle during entrainment, *J. Hydraul. Eng.* **136**, 756 (2010).
- [40] A. Dwivedi, B. Melville, A. J. Raudkivi, A. Y. Shamseldin, and Y.-M. Chiew, Role of turbulence and particle exposure on entrainment of large spherical particles in flows with low relative submergence, *J. Hydraul. Eng.* **138**, 1022 (2012).
- [41] B. Vowinckel, R. Jain, T. Kempe, and J. Fröhlich, Entrainment of single particles in a turbulent open-channel flow: A numerical study, *J. Hydraul. Res.* **54**, 158 (2016).
- [42] M. Valyrakis, P. Diplas, and C. L. Dancey, Entrainment of coarse particles in turbulent flows: An energy approach, *J. Geophys. Res.: Earth Surf.* **118**, 42 (2013).
- [43] M. Valyrakis, P. Diplas, and C. L. Dancey, Entrainment of coarse grains in turbulent flows: An extreme value theory approach, *Water Resour. Res.* **47**, W09512 (2011).
- [44] W. P. Breugem, B. J. Boersma, and R. E. Uittenbogaard, The influence of wall permeability on turbulent channel flow, *J. Fluid Mech.* **562**, 35 (2006).
- [45] P. D. Komar and Z. Li, Pivoting analysis of the selective entrainment of sediments by shape and size with application to gravel threshold, *Sedimentology* **33**, 425 (1986).
- [46] C. M. White and G. I. Taylor, The equilibrium of grains on the bed of a stream, *Proc. R. Soc. London, Sr. A* **174**, 322 (1940).
- [47] M. H. Garcia, Sediment transport and morphodynamics, in *Sedimentation Engineering: Processes, Measurements, Modeling, and Practice* (American Society of Civil Engineers, Reston, Virginia, USA, 2008), pp. 21–163.
- [48] C. Manes, D. Pokrajac, I. McEwan, and V. Nikora, Turbulence structure of open channel flows over permeable and impermeable beds: A comparative study, *Phys. Fluids* **21**, 125109 (2009).
- [49] A. F. E. Zagni and K. V. H. Smith, Channel flow over permeable beds of graded spheres, *J. Hydraul. Div.* **102**, 207 (1976).
- [50] H. J. Zippe and W. H. Graf, Turbulent boundary-layer flow over permeable and nonpermeable rough surfaces, *J. Hydraul. Res.* **21**, 51 (1983).
- [51] J. Nikuradse, *Laws of Flow in Rough Pipes* (National Advisory Committee for Aeronautics, Washington DC, 1950).
- [52] R. A. Bagnold, Fluid forces on a body in shear-flow: Experimental use of ‘stationary flow,’ *Proc. R. Soc. London A* **340**, 147 (1974).

- [53] G. Blois, G. H. S. Smith, J. L. Best, R. J. Hardy, and J. R. Lead, Quantifying the dynamics of flow within a permeable bed using time-resolved endoscopic particle imaging velocimetry (EPIV), *Exp. Fluids* **53**, 51 (2012).
- [54] G. Blois, J. L. Best, G. H. S. Smith, and R. J. Hardy, Effect of bed permeability and hyporheic flow on turbulent flow over bed forms, *Geophys. Res. Lett.* **41**, 6435 (2014).
- [55] F. Bigillon, Y. Niño, and M. H. Garcia, Measurements of turbulence characteristics in an open-channel flow over a transitionally-rough bed using particle image velocimetry, *Exp. Fluids* **41**, 857 (2006).
- [56] V. Nikora, D. Goring, I. McEwan, and G. Griffiths, Spatially averaged open-channel flow over rough bed, *J. Hydraul. Eng.* **127**, 123 (2001).
- [57] R. A. Granger, *Fluid Mechanics* (CBS College Publishing, New York, USA, 1985).
- [58] Y. Nakayama, *Introduction to Fluid Mechanics* (Butterworth-Heinemann, Kidlington, Oxford, UK, 2018).
- [59] H. A. Einstein and E.-S. A. El-Samni, Hydrodynamic forces on a rough wall, *Rev. Mod. Phys.* **21**, 520 (1949).
- [60] W. S. Chepil, The use of evenly spaced hemispheres to evaluate aerodynamic forces on a soil surface, *Trans., Am. Geophys. Union* **39**, 397 (1958).
- [61] W. S. Chepil, The use of spheres to measure lift and drag on wind-eroded soil grains I, *Soil Sci. Soc. Am. J.* **25**, 343 (1961).
- [62] A. C. Brayshaw, L. E. Frostick, and I. Reid, The hydrodynamics of particle clusters and sediment entrapment in coarse alluvial channels, *Sedimentology* **30**, 137 (1983).
- [63] A. Dwivedi, B. W. Melville, A. Y. Shamseldin, and T. K. Guha, Analysis of hydrodynamic lift on a bed sediment particle, *J. Geophys. Res.: Earth Surf.* **116**, F02015 (2011).
- [64] N. L. Coleman, A theoretical and experimental study of drag and lift forces acting on a sphere resting on a hypothetical streambed, in *Proceedings 12th Congress of the International Association for Hydraulic Research* (Fort Collins, Colorado, USA, 1967), pp. 185–192.
- [65] J. D. Fenton and J. E. Abbott, Initial movement of grains on a stream bed: The effect of relative protrusion, *Proc. R. Soc. London A* **352**, 523 (1977).